This paper appears in IEEE Robotics and Automation Letters (RA-L). 2017
DOI: 10.1109/LRA.2017.2768122

Surgeon-in-the-loop 3-D Needle Steering Through Ultrasound-guided Feedback Control

Jay Carriere[1], Mohsen Khadem[1], Carlos Rossa[1], Nawaid Usmani[2], Ronald Sloboda[2], Mahdi Tavakoli[1]

***Abstract*—Needle deflection during certain minimally invasive percutaneous procedures, such as prostate biopsy or brachytherapy, is undesired and can be reduced through the use of feedback control. This paper uses a depth-dependent reduced-order 3D nonholonomic model of needle tip motion to propose a needle deflection controller that works in a surgeon-in-the-loop fashion, where the surgeon is in charge of needle insertion, and the feedback controller is responsible for keeping the needle on its desired trajectory. The controller is based on a continuous-time control law that asymptotically brings needle deflection to zero, and is shown to remain effective even when the magnitude of the needle rotation velocity is limited. Limiting of the needle rotational velocity is due to practical considerations such as to reduce tissue damage during insertion and to show a measure of velocity-independence of the controller when high insertion speeds would require unfeasibly fast rotations. The velocity-limited controller is evaluated in three different ex-vivo tissue samples in a total of 30 needle insertion trials using real-time needle deflection measurements from ultrasound images. The ex-vivo results show an average absolute needle tip deflection of 0.54 mm away from the target location at a depth of 120 mm, and an average needle tip deflection of 0.36 mm away from the desired target axis throughout the entire insertion length.**

***Index Terms*—Medical Robots and Systems, Surgical Robotics: Steerable Catheters/Needles, Human Factors and Human-in-the-Loop, Nonholonomic Mechanisms and Systems**

I. Introduction

ROBOTIC assistance of needle-based surgeries and therapies represents a growing area of interest in medical robotics. Percutaneous procedures are used as either a diagnostic tool (e.g., in the case of biopsy) or a therapeutic tool (e.g., in the case of drug or radioactive seed delivery). In particular, robotic assistance can help to reduce needle deflection during insertion into tissue.

Manuscript received: May 23, 2017; Revised September 15, 2017; Accepted October 10, 2017.

This paper was recommended for publication by Editor Allison M. Okamura upon evaluation of the Associate Editor and Reviewers' comments. This work was supported by the Natural Sciences and Engineering Research Council (NSERC) of Canada under grant CHRP 446520, the Canadian Institutes of Health Research (CIHR) under grant CPG 127768, and by Alberta Innovates - Health Solutions (AIHS) under grant CRIO 201201232.

[1]Jay Carriere (Corresponding Author), Moshen Khadem, Carlos Rossa, and Mahdi Tavakoli are with the Department of Electrical and Computer Engineering, University of Alberta, AB, Canada T6G 1H9. jtcarrie@ualberta.ca, mohsen.khadem@ualberta.ca, carlos.rossa@uoit.ca, mahdi.tavakoli@ualberta.ca

[2]Nawaid Usmani and Ron Sloboda are with the Department of Oncology, Cross Cancer Institute, 11560 University Avenue, Edmonton, AB, Canada, T6G 1Z2. nawaid.usmani@albertahealthservices.ca, ron.sloboda@albertahealthservices.ca.

Digital Object Identifier (DOI): see top of this page.

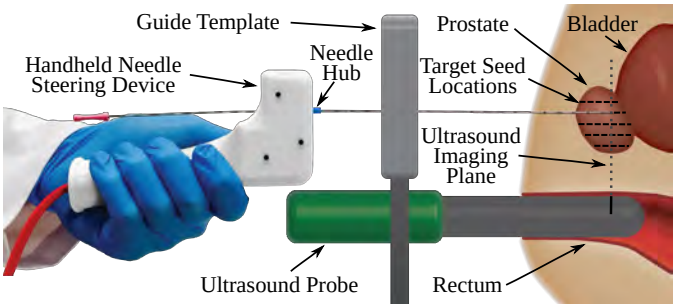

Fig. 1. Diagram of brachytherapy setup with TRUS probe, ultrasound imaging plane, needle steering device, and guide template.

The target percutaneous procedure of this paper is prostate brachytherapy, in which a clinician inserts a long flexible needle containing radioactive seeds through the perineum and into the prostate (see Fig. 1). One in eight Canadian men are diagnosed with prostate cancer in their lifetime [1]. Prostate brachytherapy is a leading option for early-stage prostate cancer treatment [2] and is of growing practical importance. During insertion, the initial placement of the needle is controlled through the use of a guide template, as illustrated in Fig. 1. The guide template consists of a series of equidistant holes that the needle passes through and that line up with the locations of pre-planned seed deposition targets with a given insertion depth. The clinician can measure the deflection of the needle tip in ultrasound images by manually stepping the ultrasound probe forward or backward with respect to the guide template.

One complication of prostate brachytherapy is that as the needle is inserted into tissue, it will deflect away from the desired straight path due to the interactions between the asymmetric needle bevel and tissue. This needle deflection causes the seed deposition locations to deviate from the pre-planned target location, which can cause suboptimal treatment of the cancerous tissue [3]. This paper focuses on reducing the deflection of the needle tip during the entire insertion; often referred to as needle deflection regulation in the literature [4]. Using a handheld motorized needle steering device [5] that acts as a robotic assistant to the surgeon, the base of the needle is automatically rotated during insertion to correct for needle deflection. This rotation changes the orientation of the needle bevel and thus the direction of needle deflection. In the context of this paper, regulation of needle tip deflection to zero across the entire length of needle insertion is desirable. Eliminating deflection during the entire insertion length is ideal for procedures such as prostate brachytherapy because

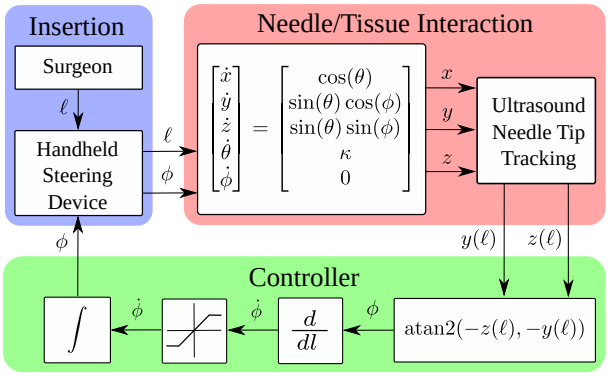

Fig. 2. Control loop diagram showing the controller outlined in this paper. Note that the value of $\dot{\phi}$ is tested to see if it is above the saturation limit; if it is beneath this limit, then the value of ϕ is sent directly to the handheld device to avoid differentiation noise

it ensures both that the needle tip will accurately reach the desired target location and that all seeds loaded into each needle are deposited on or near the desired straight line.

In this paper, we will propose and evaluate this needle deflection controller designed using a reduced-order 3D nonholonomic bicycle model; see Fig. 2. The controller is based on a switching continuous-time control law and is shown to asymptotically reduce the needle tip deflection to zero. This controller is designed within the context of surgeon-in-the-loop needle insertion, where the clinician manually inserts the needle and the controller reduces the needle deflection away from the target in 3D. The performance of the controller is evaluated with a constraint on the maximum output needle rotation velocity to show that acceptable performance is achieved under practical considerations of patient safety and to mechanical limitations on needle rotation velocity which would otherwise force a clinician to slow down the insertion.

The rest of this paper is organized as follows. Related work and an overview of the reduced nonholonomic bicycle model is outlined in Sec. II. The controller is developed in Sec. III. The experimental setup for evaluating the controller is presented in Sec. IV with the results of the ex-vivo tissue trials using the handheld device given in Sec. V. The conclusions and future work will be summarized in Sec. VI.

II. Background

The bicycle model is typically applied to the control of mobile robots. However, [6] and [7] modified it to describe the motion of a beveled-tip needle as it is inserted into tissue. This model has been used quite often in the literature for needle trajectory control. Research in [7] applied this needle deflection model to control a needle directed toward a target in a single 2D plane. One complication of using the bicycle model is that it is non-trivial to estimate the system states in real-time control. Our previous work [8] developed a particle filter based technique for state estimation of a 2D variable plane bicycle model from clinical ultrasound images insertion images in real-time and [9] showed that an Unscented Kalman Filter may be used for 3D state estimation. Using modern control techniques, the researchers in [10] developed a linearizing transform for a 2D version of the bicycle model and implemented it in an observer-controller combination. Sliding mode control has also proven very effective at the combination of state-estimation and control applied to the bicycle model with [11] implementing 2D and [12] implementing 3D sliding mode controllers. One contribution of the controller presented in this paper is that it is proved to asymptotically converge based only on needle deflection measurements and does not require any state estimation.

The bicycle model has also been used for trajectory control in 3D by modeling the needle deflection over small insertion lengths as being contained in a number of 2D planes with [13] and [14] developing trajectory controllers to compensate for 3D target motion and account for 3D obstacle motion inside tissue. This is similar to the work of [15] where ultrasound image tracking was used along with the bicycle model for needle steering in the presence of tissue motion. The constant curvature model has also been augmented with mechanical needle characteristics in [16] for control of the needle trajectory. This work was extended to consider the interaction of needle and tissue mechanics by [17] and [18]. While not unique to this work, the controller presented here is capable of 3D needle control without constraining the needle motion to be in planar segments and with negligible computational time to calculate the control output when compared to mechanical model-based control.

This paper will use a reduced-order nonholonomic model originally presented in [19] for control of a needle in 3D by feedback-linearization in a Frenet-Serret frame. This work will build on this model and use it for feedback control of the needle tip deflection in a general 3D frame. This model assumes that the needle is stiff in both torsional and compressional directions such that insertion and rotation at the base of the needle are conveyed directly to the needle tip.

A. Reduced Order Bicycle Model

From the work of [19], the derivation of the reduced-order model uses an inertial frame $\{0\}$ anchored at the point of needle insertion into tissue and a frame $\{T\}$ that is rigidly attached to the tip of the needle as shown in Fig. 3. At the beginning of insertion, the two frames coincide. The needle base velocity along the direction of insertion is denoted as v, and rotational velocity on the needle base is indicated by w, where $v, w \in \mathbb{R}$. The axes of the inertial frame, labeled $[{}^0x', {}^0y', {}^0z']$, are stationary at the point of needle exit out of the guide template and define the coordinates of the 3D space. The tip-attached frame $\{T\}$ is placed such that the origin of the frame is at the needle tip, with the axes of this frame denoted by $[{}^Tx', {}^Ty', {}^Tz']$. During insertion, the insertion base velocity v will translate the needle tip along the ${}^Tx'$ axis. The position of the needle tip (and equivalently the origin of frame $\{T\}$), with respect to the base frame $\{0\}$, is given by $p = [x, y, z] \in \mathbb{R}^3$. The Tait-Bryan angle definition of rotation about the Z-Y-X axes, involving the angles ψ, θ, ϕ, is used to represent the rotational orientation of frame $\{T\}$ with respect to frame $\{0\}$.

In this model, we assume that the needle is torsionally stiff such that rotation of the needle base is conveyed directly to

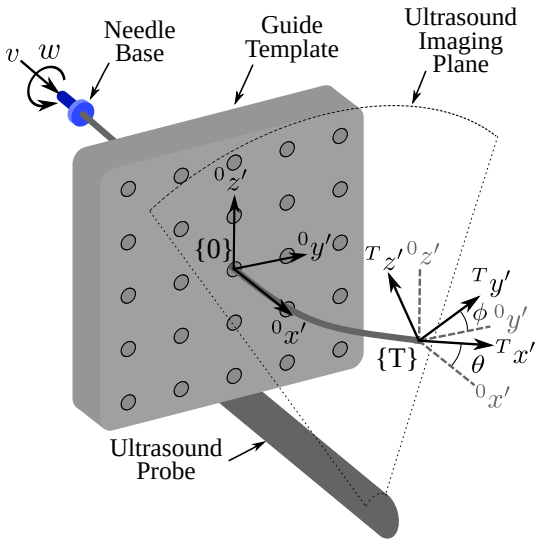

Fig. 3. Coordinate system used for kinematic model of needle motion, showing TRUS probe, axial imaging plane, control inputs and needle base, and guide template.

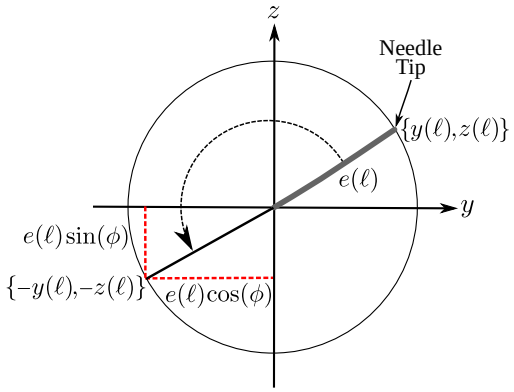

Fig. 4. Axial view (along x-axis viewed from the needle tip) of needle deflection with switching control action.

the needle tip. From this torsional stiffness, a rotation at the base of the needle with an input rotational velocity of w, about the $^0x'$ axis, is the same as directly rotating the needle bevel implying the tip-attached frame rotates about $^Tx'$ with the same input w velocity. The angle of rotation about $^Tx'$, with respect to the orientation of $\{0\}$, is defined as ϕ where $\{\phi \in \mathbb{R} : -\pi \leq \phi < \pi\}$.

The angle ϕ is related to the physical orientation of the asymmetric bevel on the needle-tip and, in an analogous manner to the work of [6] and [7], we model the needle-tissue interaction as causing a constant "turning" action of the needle tip frame. Here, we define $\{T\}$ to be attached such that the needle bending is modeled as a rotation of the frame $\{T\}$ about the axis $^Ty'$. The angle θ, where $\{\theta \in \mathbb{R} : 0 \leq \theta < \pi\}$, represents the angle of this rotation. The rate of change in the angle θ is defined as the variable κ, where κ represents the inverse of the radius of curvature of the needle and is constant during insertion ($\kappa = \frac{1}{R}$). Thus controlling the angle of ϕ changes the orientation of the $^Ty'$ axis and steers the needle.

With the torsional stiffness assumption implying direct control of the needle bevel about $^Tx'$ and by defining needle bending as a rotation about $^Ty'$ it follows that there is no action which will cause the needle tip to be rotated about the $^Tz'$ axis. This stiffness assumption is valid, as shown in [19], for the 18-gauge stainless steel needles used in this work as well and in clinical brachytherapy. This assumption may not hold for substantially thinner or more flexible needles such as those made out of nitinol (where effects such as torsional windup can be modeled as causing a rotation about $^Tz'$). We thus consider the angle of rotation about the $^Tz'$ axis to be zero in this model, therefore $\psi = 0$, and so the system reduces to 5-DoF. The states of the reduced-order system are then given as $X = [x, y, z, \theta, \phi]$.

A full derivation of the model is given in [19] along with proofs of accessibility and controllability. As the goal is to use a handheld device for surgeon-in-the-loop cooperative needle insertion, we would prefer to have our model, and therefore the control action, written as a function of the inserted length of the needle ℓ rather than insertion time. To do this, motivated by [10], a division of the entire system by the needle base velocity v is performed, noting that $v = \frac{d\ell}{dt}$. The result is a depth-dependent nonholonomic system described by

$$\dot{X} = \begin{bmatrix} \dot{x} \\ \dot{y} \\ \dot{z} \\ \dot{\theta} \\ \dot{\phi} \end{bmatrix} = \begin{bmatrix} \cos(\theta) \\ \sin(\theta)\cos(\phi) \\ \sin(\theta)\sin(\phi) \\ \kappa \\ 0 \end{bmatrix} + \begin{bmatrix} 0 \\ 0 \\ 0 \\ 0 \\ 1 \end{bmatrix} w \qquad (1)$$

Here, in a slight abuse of notation which we shall use throughout the rest of this paper, we use the dot operator to denote the derivative with respect to inserted needle length rather than time, such that $\dot{X} = \frac{dX}{d\ell}$. Using this depth-dependent model, we will design a controller to minimize the needle tip deflection during insertion.

III. Switching Controller

With the depth-dependent kinematic needle model outlined in Sec. II, we will design a switching control law to regulate the needle deflection away from the target $^0x'$ axis to zero, thus minimizing $e(\ell)$ at all depths during insertion where

$$e(\ell) = \sqrt{y(\ell)^2 + z(\ell)^2} \qquad (2)$$

Here, $y(\ell)$ and $z(\ell)$ are the needle tip deflections along the $^0y'$ and $^0z'$ axes respectively. This deflection measure will be used to design and evaluate the controller performance in the system. Here, the surgeon is manually inserting the needle and therefore directly controlling ℓ. With reference to Sec. II-A, as the needle is being inserted it translates the needle tip-attached frame $\{T\}$ forward along the $^Tz'$ axis. The surgeon will stop the insertion when the needle tip has reached the desired target depth on the $^0x'$ axis, thus completely controlling the position of the needle tip p in 3D space.

From (1), it is clear that one of the major advantages of this model over the standard 6-DoF model presented in the

literature is that we have the ability to directly design the value of $\phi(\ell)$ (as the control action) at a particular insertion depth, rather than having to design its derivative $\dot{\phi}(\ell)$. Consider the control law

$$\phi(\ell) = \text{atan2}(-z(\ell), -y(\ell)) \tag{3}$$

where atan2 is the four-quadrant inverse tangent function. One important note is that the reduced-order model, like the general 6-DoF model, violates Brockett's condition [20] and so cannot be stabilized with a smooth continuous controller. Thus, the atan2 function acts in this context as a switching controller. With the goal of bringing the needle tip deflection in the ${}'^0y'^0z'$-plane to zero, we shall look at a positive-definite Lyapunov function candidate $V(y,z)$ given as

$$V(y,z) = \frac{1}{2}y(\ell)^2 + \frac{1}{2}z(\ell)^2 \tag{4}$$

The derivative of this function is

$$\dot{V}(y,z) = \dot{y}(\ell)y(\ell) + \dot{z}(\ell)z(\ell) \tag{5}$$

Which, with the control law given in (3), will be shown to be negative-definite, i.e., $\dot{V}(0,0) = 0$ and $\dot{V}(x,y) < 0$, $\forall y, z \in \mathbb{R}$. By substituting our control law ϕ into the above, we have

$$\dot{V}(y,z) = sin(\theta(\ell))\cos(\phi(\ell))y(\ell) + sin(\theta(\ell))\sin(\phi(\ell))z(\ell) \tag{6}$$

Here $sin(\theta(\ell))$ is a positive number during insertion as $0 \leqslant \theta(\ell) < \pi$ from the coordinate system definition and with $\dot{\theta} = \kappa$, where κ is a positive number. Taking the current needle tip deflection as $e(\ell) = \sqrt{y(\ell)^2 + z(\ell)^2}$ we can use the trigonometric definitions

$$\cos(\phi(\ell)) = \frac{-y(\ell)}{e(\ell)} \tag{7}$$

$$\sin(\phi(\ell)) = \frac{-z(\ell)}{e(\ell)} \tag{8}$$

and substitute these into (6) resulting in

$$\begin{aligned}\dot{V}(y,z) &= sin(\theta(\ell))\left(\frac{-y(\ell)^2}{e(\ell)} + \frac{-z(\ell)^2}{e(\ell)}\right) \\ &= sin(\theta(\ell))\left(-\frac{y(\ell)^2 + z(\ell)^2}{e(\ell)}\right) \\ &= -sin(\theta(\ell))\sqrt{y(\ell)^2 + z(\ell)^2}\end{aligned} \tag{9}$$

which is a negative definite function. Therefore, using this controller, the tip needle deflection asymptotically converges to zero. As shown in the experimental results, Sec. V, this proof of convergence is conservative as in practice the system can reduce and regulate needle deflection over short needle insertion distances.

A. Practical Switching Controller

It is clear from the formulation of the switching controller that the control output $\phi(\ell)$ instantaneously turns the needle bevel 180 degrees. Implementing the controller would then require a sufficiently high rotational velocity $\dot{\phi}(\ell)$ to achieve near-ideal performance. The handheld needle steering device, or any other device used to implement the control action, will have some maximum rotation speed limit. Here, and throughout this section when referring to rotation we use speed to imply rotation in the time domain ($\frac{rad}{s}$) and velocity to refer to rotation in the insertion-depth domain ($\frac{rad}{mm}$). To implement large rotation velocities required by the ideal controller the needle insertion can be stopped or slowed during the rotation action. Thus the rotation speed of the system with respect to change in insertion depth will result in a large, or infinite, rotation velocity $\dot{\phi}(\ell)$. For this, the surgeon could be signaled to temporarily stop or slow insertion to meet the rotational velocity requirements. This would have the effect of lengthening the procedure time and would be relativity impractical.

Instead of relying on the surgeon to control insertion speed, we will modify the controller to limit the required rotation velocity. This is beneficial for practical implementation of the system as the reduced rotational velocity requirement will allow for much higher insertion velocities without being limited by the rotation speed of the needle steering device. More importantly, we want to limit the rotation velocity for patient safety. This is to prevent the controller from performing high velocity rotations, corresponding to a large $\dot{\phi}(\ell)$, over the entire insertion length. This would result in a "drilling motion", which would induce unnecessary tissue trauma. Thus we will modify the controller to limit the rotation velocity. In an attempt to bound $\dot{\phi}(\ell)$, we shall incorporate the following control limiting rule where v_{max} is the maximum admissible rotation velocity:

$$\begin{aligned}\dot{\phi}(\ell) &= \text{sat}(v_{max}, \frac{d}{dl}\text{atan2}(-z(\ell), -y(\ell))) \\ &= \text{sat}(v_{max}, \frac{\dot{z}(\ell)y(\ell) - \dot{y}(\ell)z(\ell)}{y(\ell)^2 + z(\ell)^2})\end{aligned} \tag{10}$$

with the definition of the sat function given by $\text{sat}(x,y) = \text{sign}(y)\min(x, \text{abs}(y))$. Integrating $\dot{\phi}(\ell)$ will give the actual control input to be applied to the system. Note that in the case that $|\dot{\phi}(\ell)| < v_{max}$ then control signal $\phi(\ell) = \text{atan2}(-z(\ell), -y(\ell))$ will be feed directly into the handheld controller to avoid differentiation noise.

To confirm that the controller performance is still acceptable even when $\dot{\phi}(\ell)$ is saturated (the "practical controller"), the closed-loop system was simulated in 3D for various values of v_{max}. One performance measure that was evaluated is the additional insertion length required for the controller to bring the deflection to zero when compared to the insertion length required by the controller in which $\dot{\phi}(\ell)$ was not saturated (the "ideal controller"); this measure is denoted by Δl. The other metric used was the increase in total needle deflection, $e(\ell) = \sqrt{y(\ell)^2 + z(\ell)^2}$, when compared to the ideal controller, denoted by Δe_{max}. Both of these metrics are illustrated in Fig. 5 for a simulated needle insertion.

To test the performance of the saturated controller, needle insertion was simulated 10,000 times while varying the values of both v_{max} and θ_0. Here we define the variable θ_0 to be the initial value of θ when the needle is first inserted into tissue, i.e. $\ell = 0$, such that $\theta_0 \equiv \theta(0)$. The value of v_{max} was varied from $0.1\frac{rad}{mm}$ to $0.9\frac{rad}{mm}$ and θ_0 was varied from 0° to 10°. Note that the unit of rotational velocity, $\frac{rad}{mm}$, refers to the amount of needle rotation per mm of inserted needle length as

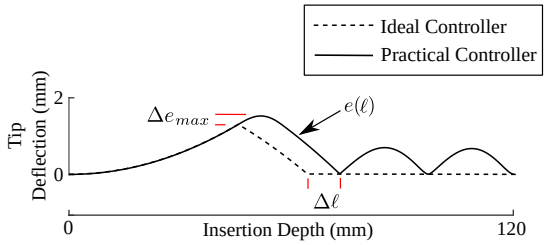

Fig. 5. Diagram of two performance measures used to evaluate the saturated controller.

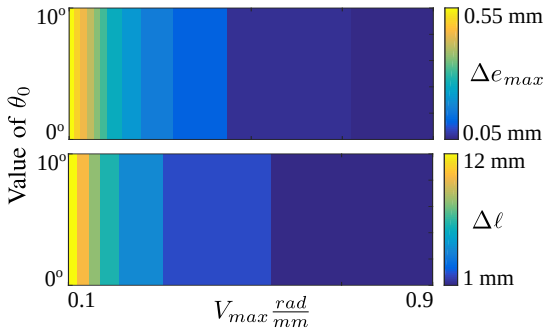

Fig. 6. Performance of controller when rotational velocity is limited.

the system model, (1), was derived to depend only on insertion depth. For the simulations, the value of κ was kept constant at $\kappa = \frac{1}{1000}$. Previously and during experiments, we had found the values of θ_0 and κ to be inside the above-reported ranges used in simulations. The result of these simulations, shown in Fig. 6, indicate that the practical controller performance approaches the performance of the ideal controller when as v_{max} is increased. The results also show that the relative performance of the practical controller is not sensitive to the changing values of θ_0. Additionally, this modified controller offers acceptable performance while being limited to low rotation velocities. This implies a manner of insertion-velocity independence where a practical needle steering system, with a finite maximum rotation speed, can provide the necessary rotation velocity for control over a broad range of insertion velocities.

IV. Experimental Setup and Ultrasound Image Processing

Needle insertions into phantom tissue were used to experimentally validate the saturated controller performance. The experimental setup, shown in Fig. 7, consisted of an ultrasound probe, prostate brachytherapy needles, three phantom tissues, and the handheld needle steering device originally presented in [5]. For the needles in the experiments, standard 200 mm long prostate brachytherapy 18-gauge seeding needles (Eckert & Zielger BEBIG GmbH, Berlin, Germany) were used.

The ultrasound machine used was an Ultrasonix Touch with a 4DL14-5/38 Linear 4D transducer (Ultrasonix Corp, Richmond, BC, Canada). Measuring the inserted length of the needle is done by using a Micron Tracker (HX60 from Claron Technology Inc., Toronto, ON, Canada) as optical tracking markers were placed on the handheld device. The needle base

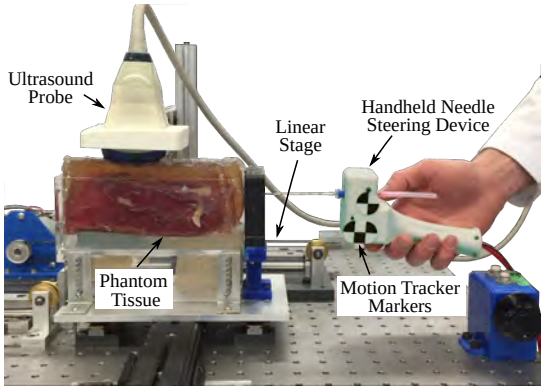

Fig. 7. Photo of experimental setup showing phantom tissue, handheld needle steering device with motion tracker markers, and ultrasound probe on motorized linear stage.

was rotated during insertion by the use of the handheld steering device.

For the ex-vivo tissue, phantoms incorporating three different materials were used. Two biological tissue phantoms contained bovine rump tissue and porcine loin tissue embedded in gelatin (Knox from Kraft Inc., Northfield, IL, USA) to represent non-homogeneous tissue that closely resembles in-vivo human tissue in both mechanical properties as well as ultrasound imaging characteristics. The other tissue phantom is made from a plastisol gel (M-F Manufacturing Co, Fort Worth, USA) that was created to test the response of the controller in materials that are stiffer and have more friction than human tissues (which makes the needle steering more challenging). The image processing and needle control routines were both coded in Matlab 2016a (The Mathworks Inc, Natwick, MA, USA) and were run on a single core of an Intel Core i7-3930K processor running at 3.20 GHz (Intel Corporation, Santa Clara, CA, USA).

For these experiments, 2D ultrasound images were used to track the needle tip during insertion. The needle tracking was done using a slightly modified version of the needle tracking algorithm presented in [21]. During insertion, ultrasound images are captured and processed in real-time (see Fig. 9a) at a frame rate of 20 Hz. Each ultrasound image is enhanced to increase the brightness of the image pixels corresponding to the needle cross section and to reduce the intensity of the background pixels representing the surrounding tissue.

In the first frame of the live ultrasound image sequence, corresponding to when the needle is just inserted, a user clicks on the center of the needle cross-section in the ultrasound image. The needle cross-section, in this work capturing the needle tip, is tracked using a template patch of pixels around it. Based on concepts from video tracking the cross-section location in the next ultrasound image frame is calculated by using normalized cross correlation (NCC) along with the assumption that the needle tip motion between frames is small. The result of the image processing and needle tip tracking patch is seen in Fig. 9b. During insertion, the ultrasound imaging probe translates forward along the axis of needle insertion ${}^0x'$, using the motion tracker measurement of ℓ, so that the needle tip is always captured in the image plane.

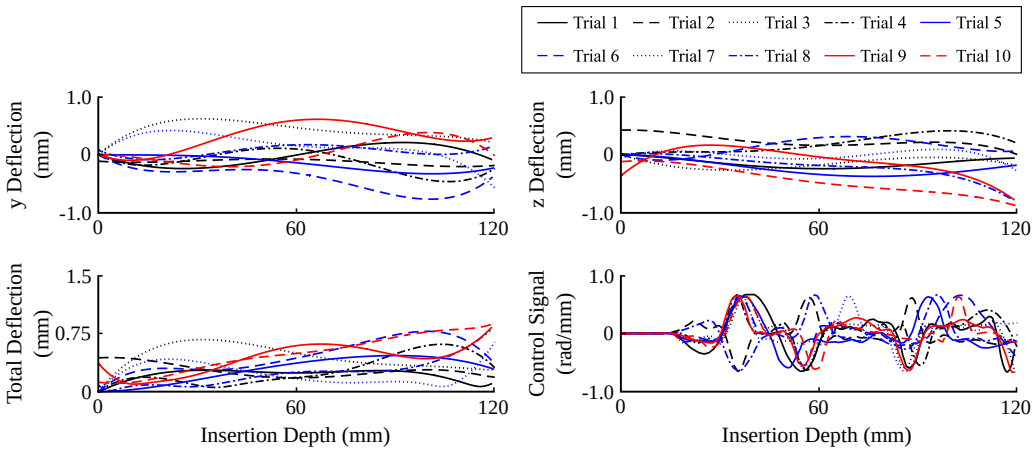

(a) Needle tip path, total deflection, and steering control signal in porcine tissue.

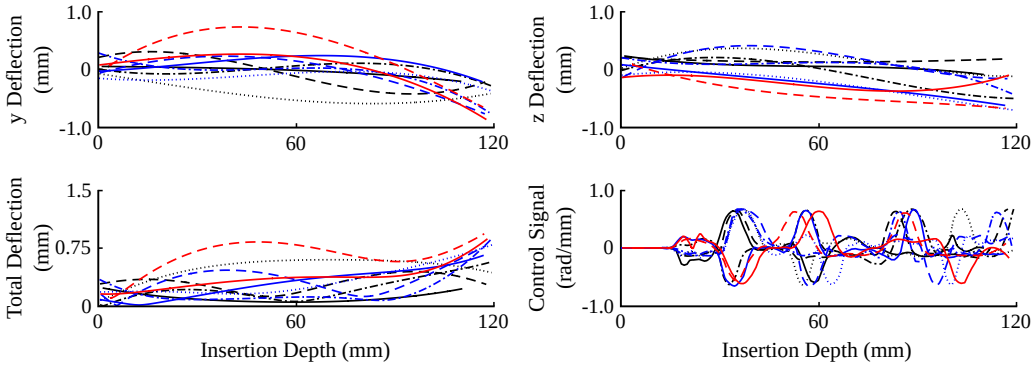

(b) Needle tip path, total deflection, and steering control signal in bovine tissue.

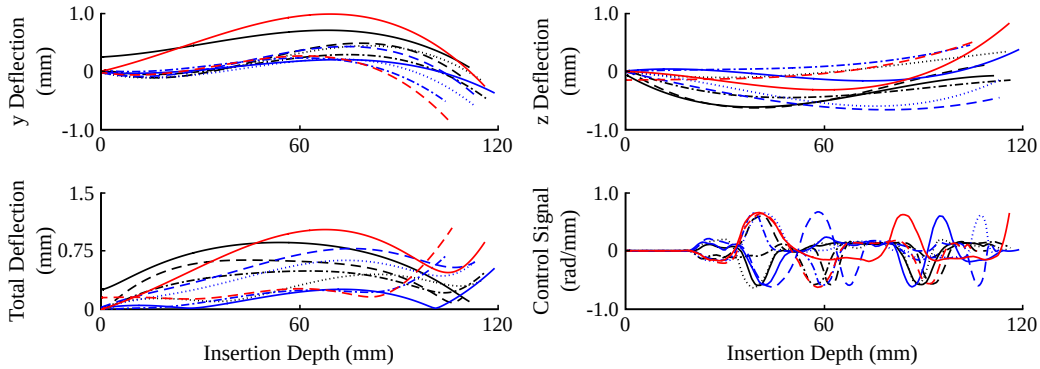

(c) Needle tip path, total deflection, and steering control signal in plastisol tissue.

Fig. 8. Results of needle insertion experiments in the three phantom tissues.

The pixel coordinate output of the tracking routine was then converted to the needle tip location in the ${}^0y'\,{}^0z'$-plane in real-world mm coordinates. The ultrasound image pixel coordinates were calibrated to provide accurate real-world measurements throughout the entire insertion. The calibration was performed by taking four image points with measured real-world coordinates, manually selected in two ultrasound image slices at insertion depths of 10 mm and 100 mm respectively. This image-metric calibration was done individually for each of the three tissues to compensate for speed of sound differences.

For the controller, only information about the current needle tip coordinates $y(\ell)$ and $z(\ell)$ is required. One complication, however, is that the needle tip position as returned from the ultrasound images will contain a large amount of positional noise (or jitter) due to the low spatial resolution of ultrasound images and signal-to-noise similarities between the needle and background tissue. In order to combat this, we use a simple noise filtering routine using a linear Kalman filter on the positional data to estimate the true needle position in the current frame.

V. Results

For each of the three previously described tissue phantoms, ten insertion trials were completed, and the efficacy of the controller was evaluated by looking at two metrics. For each

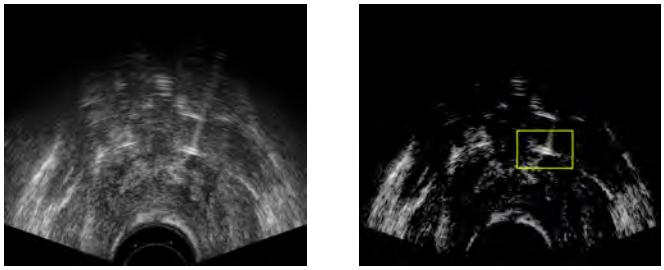

(a) (b)

Fig. 9. Ultrasound image processing showing original input image and variance image with tracking area.

trial the target location was chosen to correspond to real-world ${}^0y'\,{}^0z'$-plane coordinate of the center of a hole in the guide template, see Fig. 3, at a depth of 120 mm. The needle was allowed to deflect in an uncontrolled manner for the first 20 mm of insertion to evaluate the efficacy of the controller at regulating needle deflection in the presence of some initial deflection from the target axis. Additionally, the results presented here show the real-world deflection in mm, measured via calibrated ultrasound images. The needle deflection is shown relative to the target axis and any initial needle tip offset from the target axis, caused by tissue motion during insertion, was not compensated for to provide a fair comparison with the insertion errors seen in current clinical practice.

Once the needle had been inserted to a depth of 20 mm the control output was applied and the handheld device rotated the needle during the remaining 100 mm of insertion. For these results, the rotational velocity of the system was constrained to be under ± 0.65 rad/mm using the methodology developed in Sec. III-A. A buzzer was used to indicate to the user that the target depth had been reached. The insertion speed of the needle was not controlled and the insertion depth was captured in real-time using the Micron Tracker.

The needle tip position in the ${}^0y'\,{}^0z'$-plane, measured in ultrasound images, was used as the feedback to the controller. The two metrics used to evaluate the efficacy of the controller are based on the Euclidean distance of the needle tip away from the target ${}^0x'$-axis. The first metric is based on the definition of $e(\ell)$, given in (2), and evaluated the deflection of the needle tip when fully inserted into tissue, given by

$$\text{Final Tip Deflection} = \sqrt{y(\ell)^2 + z(\ell)^2} \tag{11}$$

where L is the depth of the needle tip at the end of the insertion. Given that the goal of the controller was to limit needle tip deflection during the entire insertion length, the second measure is defined as

$$\text{Mean Tip Deflection} = \sum_{i=0}^{L} \frac{\sqrt{y(i)^2 + z(i)^2}}{n} \tag{12}$$

where $y(i)$ and $z(i)$ denote the needle tip deflection measured in an ultrasound image frame at a discrete depth i during insertion and n is the total number of discrete depth points captured during insertion. For the Mean Tip Deflection results given in Table I the $y(\ell)$ and $z(\ell)$ coordinate found in the ultrasound image slice nearest to 100 equally spaced points along the ${}^0x'$-axis (from 0 mm to final insertion depth) were used, such that $n = 100$. The result of the needle insertion experiments is given in Table I, with the values in each row corresponding to the averaged final tip deflection and averaged mean tip deflection, along with respective standard deviations for the ten trials in each tissue. The largest values across the 10 trials are given in maximum final tip deflection and maximum mean insertion tip deflection. The measured needle deflection for each of the insertions was plotted with respect to insertion depth. The experimental data was smoothed by fitting the measured deflection for the entire insertion to a 3rd order polynomial which was constrained such that the polynomial curve exactly matched experimental deflection measured at the initial insertion depth (0 mm) and the final insertion depth. The results for the porcine tissue phantom given in Fig. 8a, the bovine tissue phantom in Fig. 8b, and the plastisol tissue phantom in Fig. 8c. In the context of surgeon-in-the-loop needle steering, an important criterion is that the controller is robust to changes in insertion speed. To this end, insertion speed was not controlled during the experimental trials but was measured for each of trails. For the porcine tissue insertion the maximum insertion velocity measured was 41 mm/s with an average insertion velocity of 9.5 mm/s, for the bovine tissue the maximum insertion velocity measured was 52 mm/s with an average insertion velocity of 9.4 mm/s, and for the plastisol tissue the maximum insertion velocity measured was 35 mm/s with an average insertion velocity of 8.5 mm/s

TABLE I
EXPERIMENTAL RESULTS

	Final Tip Deflection	Standard Deviation	Mean Tip Deflection	Standard Deviation
Porcine Tissue	0.47 mm	0.29 mm	0.35 mm	0.10 mm
Bovine Tissue	0.64 mm	0.25 mm	0.51 mm	0.19 mm
Plastisol Tissue	0.51 mm	0.27 mm	0.39 mm	0.15 mm

	Maximum Final Tip Deflection	Maximum Total Tip Deflection
Porcine Tissue	0.90 mm	0.55 mm
Bovine Tissue	0.93 mm	0.52 mm
Plastisol Tissue	1.04 mm	0.57 mm

From results in Table I, we can see that the performance of the controller is relatively insensitive to the tissue characteristics with all 30 insertions having an average final tip deflection of 0.54 $\pm$ 0.27 mm and an average total tip deflection of 0.36 $\pm$ 0.12 mm. Of note is the higher total tip deflection and maximum final tip deflection in plastisol, which is primarily due to the unrealistically high values of needle-tissue friction and stiffness in this tissue that increases the needle deflection during insertion. The maximum target error of 1.04 mm is still beneath the average targeting error of 1.22 reported in [4] for other 2D and 3D needle steering algorithms and is significantly better than the 5 mm accuracy reported clinically for conventional (i.e., non-robotic) prostate brachytherapy [22].

VI. Conclusion

In this paper, we have presented a surgeon-in-the-loop needle steering controller for percutaneous procedures that is designed to regulate to zero the needle tip deflection. The controller was based on a reduced-order kinematic bicycle model and has been modified to depend only on the inserted depth of the needle, which can readily be measured externally, and using needle tip position feedback from an ultrasound imaging device without requiring significant changes to the current clinical operating procedure. The rotation of the needle tip, corresponding to the model control input, was done using a light-weight and clinician-friendly handheld device that allows the surgeon to fully carry out the needle insertion and decide the final insertion depth.

The controller has been shown to asymptotically bring the needle deflection error to zero in the ideal case. A practical variant of the controller that limits the needle rotation speed for both mechanical and tissue damage reduction effects was implemented. The stability and performance of the practical controller is evaluated both in simulation as well as experimentally in ex-vivo tissue phantoms. The experimental results from the ex-vivo phantoms, created from bovine, porcine, and plastisol tissues, show that the controller is robust with respect to both non-homogeneous tissue as well as varying tissue types. The average targeting error in across all of the needle insertion experiments in the three tissues resulted in an average final needle tip deflection of 0.54 ± 0.27 mm and an average total tip deflection of 0.36 ± 0.12 mm throughout the entire insertion. While this work was presented in the context of prostate brachytherapy, it could be useful for any percutaneous procedure that requires precise needle placement with ultrasound image-guided feedback.

Future work will involve state estimation of the reduced-order kinematic model, allowing for predictive control of the needle deflection as well as paving the way for further reducing the number and frequency of needle rotations required to minimize the needle deflection. Additional work could involve magnetic position sensing of the needle tip, thereby removing the requirement for passive tracking markers on the handheld device as well as ultrasound image feedback. The real-time response of the needle controller and ultrasound image processing allow for the current system to be tested in more standard clinical environments, and future work will evaluate the performance benefits of such a device when used by a skilled clinician.

References

[1] Canadian Cancer Societys Steering Committee, "Canadian Cancer Statistics," 2015, [Online]. Available: http://www.cancer.ca/statistics.

[2] D. Bowes and J. Crook, "A critical analysis of the long-term impact of brachytherapy for prostate cancer: a review of the recent literature." *Current Opinion in Urology*, vol. 21, no. 3, pp. 219 – 224, 2011.

[3] J. E. Dawson, T. Wu, T. Roy, J. Y. Gu, and H. Kim, "Dose effects of seeds placement deviations from pre-planned positions in ultrasound guided prostate implants." *Radiotherapy And Oncology: Journal Of The European Society For Therapeutic Radiology And Oncology*, vol. 32, no. 3, pp. 268 – 270, 1994.

[4] C. Rossa and M. Tavakoli, "Issues in closed-loop needle steering," *Control Engineering Practice*, vol. 62, pp. 55 – 69, 2017.

[5] C. Rossa, N. Usmani, R. Sloboda, and M. Tavakoli, "A hand-held assistant for semiautomated percutaneous needle steering," *IEEE Transactions on Biomedical Engineering*, vol. 64, no. 3, pp. 637–648, March 2017.

[6] W. Park, J. S. Kim, Y. Zhou, N. J. Cowan, A. M. Okamura, and G. S. Chirikjian, "Diffusion-based motion planning for a nonholonomic flexible needle model," in *Proceedings of the 2005 IEEE International Conference on Robotics and Automation*, April 2005, pp. 4600–4605.

[7] R. J. Webster, J. S. Kim, N. J. Cowan, G. S. Chirikjian, and A. M. Okamura, "Nonholonomic modeling of needle steering," *The International Journal of Robotics Research*, vol. 25, no. 5-6, pp. 509–525, 2006.

[8] J. Carriere, C. Rossa, R. Sloboda, N. Usmani, and M. Tavakoli, "Real-time needle shape prediction in soft-tissue based on image segmentation and particle filtering," in *2016 IEEE International Conference on Advanced Intelligent Mechatronics (AIM)*, July 2016, pp. 1204–1209.

[9] T. K. Adebar and A. M. Okamura, "Recursive estimation of needle pose for control of 3d-ultrasound-guided robotic needle steering," in *2014 IEEE/RSJ International Conference on Intelligent Robots and Systems*, Sept 2014, pp. 4303–4308.

[10] V. Kallem and N. Cowan, "Image guidance of flexible tip-steerable needles," *IEEE Transactions on Robotics*, vol. 25, no. 1, pp. 191–196, Feb 2009.

[11] B. Fallahi, C. Rossa, R. S. Sloboda, N. Usmani, and M. Tavakoli, "Sliding-based image-guided 3D needle steering in soft tissue," *Control Engineering Practice*, vol. 63, pp. 34 – 43, 2017.

[12] D. C. Rucker, J. Das, H. B. Gilbert, P. J. Swaney, M. I. Miga, N. Sarkar, and R. J. Webster, "Sliding mode control of steerable needles," *IEEE Transactions on Robotics*, vol. 29, no. 5, pp. 1289–1299, Oct 2013.

[13] G. J. Vrooijink, M. Abayazid, S. Patil, R. Alterovitz, and S. Misra, "Needle path planning and steering in a three-dimensional non-static environment using two-dimensional ultrasound images," *The International Journal of Robotics Research*, vol. 33, no. 10, pp. 1361–1374, 2014.

[14] S. Patil, J. Burgner, R. J. Webster, and R. Alterovitz, "Needle steering in 3-D via rapid replanning," *IEEE Transactions on Robotics*, vol. 30, no. 4, pp. 853–864, Aug 2014.

[15] R. Alterovitz, M. Branicky, and K. Goldberg, "Motion planning under uncertainty for image-guided medical needle steering," *The International Journal of Robotics Research*, vol. 27, no. 11-12, pp. 1361–1374, 2008.

[16] N. Abolhassani, R. Patel, and F. Ayazi, "Needle control along desired tracks in robotic prostate brachytherapy," in *Systems, Man and Cybernetics, 2007. ISIC. IEEE International Conference on*, Oct 2007, pp. 3361–3366.

[17] S. Misra, K. Reed, B. Schafer, K. Ramesh, and A. Okamura, "Mechanics of flexible needles robotically steered through soft tissue." *International Journal of Robotics Research*, vol. 29, no. 13, pp. 1640 – 1660, 2010.

[18] P. Moreira and S. Misra, "Biomechanics-based curvature estimation for ultrasound-guided flexible needle steering in biological tissues," *Annals of Biomedical Engineering*, vol. 43, no. 8, pp. 1716–1726, 2015. [Online]. Available: http://dx.doi.org/10.1007/s10439-014-1203-5

[19] M. Khadem, C. Rossa, N. Usmani, R. S. Sloboda, and M. Tavakoli, "Feedback-linearization-based 3D needle steering in a frenet-serret frame using a reduced order bicycle model," in *2017 American Control Conference (ACC)*, May 2017, pp. 1438–1443.

[20] D. Liberzon, *Switching in Systems and Control*, 1st ed. Boston, MA: Birkhuser Basel, 2003.

[21] J. Carriere, C. Rossa, N. Usmani, R. Sloboda, and M. Tavakoli, "Needle shape estimation in soft tissue based on partial ultrasound image observation," in *Robotics and Automation (ICRA), 2015 IEEE International Conference on*, May 2015, pp. 2277–2282.

[22] M. F. Jamaluddin, S. Ghosh, M. P. Waine, R. S. Sloboda, M. Tavakoli, J. Amanie, A. D. Murtha, D. Yee, and N. Usmani, "Quantifying ^{125}I placement accuracy in prostate brachytherapy using postimplant transrectal ultrasound images," *Brachytherapy*, vol. 16, no. 2, pp. 306 – 312, 2017.